Special Collection

Probing the Effects of Electron Deficient Aryl Substituents and a π-System Extended NHC Ring on the Photocatalytic CO_2 Reduction Reaction with Re-pyNHC-Aryl Complexes**

Hunter Shirley[+],[a] Thomas More Sexton[+],[a] Nalaka P. Liyanage,[a] Morgan A. Perkins,[a] Shane A. Autry,[a] Louis E. McNamara,[a] Nathan I. Hammer,[a] Sean R. Parkin,[b] Gregory S. Tschumper,*[a] and Jared H. Delcamp*[a]

The ever-expanding need for renewable energy can be addressed in part by photocatalytic CO_2 reduction to give fuels via an artificial photosynthetic process driven by sunlight. A series of rhenium photocatalysts are evaluated in the photocatalytic CO_2 reduction reaction and via photophysical, electrochemical, and computational studies. The impact of various electron withdrawing substituents on the aryl group of the pyNHC-aryl ligand along with the impact of extending conjugation along the backbone of the ligand is analyzed. A strong correlation between excited-state lifetimes, photocatalytic rates, and computationally determined dissociation energy of the labile ligand of these complexes is observed. Additionally, computed orbital analysis provides an added understanding, which allows for prediction of the potential impact of an electron withdrawing substituent on photocatalysis.

1. Introduction

Converting CO_2 waste to a usable fuel source is an attractive avenue for both the future of renewable energy and for reducing anthropogenic CO_2 output.[1] Photocatalysts offer the opportunity to directly reduce CO_2 to valuable fuel precursors by utilizing visible light given off by the earth's most abundant energy source, the Sun. Molecular photocatalysts are readily tunable with regard to rate and durability of the photocatalytic CO_2 reduction reaction (PCO_2RR).[1e,2] The direct use of sunlight at a single metal complex to drive the PCO_2RR is relatively rare and forgoes the need of additional electron transfers from a photosensitizer, resulting in a fundamental advantage in terms of free-energy conservation.

NHC (*N*-heterocyclic carbene) ligands have been shown to improve catalyst durability.[3] In general, Re-NHC complexes have shown intriguing photophysical properties.[4] Additionally, the strong electron donating properties of these ligands to the metal center may assist in enhancing the rate of the CO_2 reduction reaction (CO_2RR).[5] As an example, the well-known Re(bpy)$(CO)_3$Br (**1**, where bpy is 2,2′-bipyridine) benchmark PCO_2RR catalyst is surpassed in rate by the introduction of an NHC group to give Re(pyNHC-PhCF_3)$(CO)_3$Br (**2**, where py is pyridine) (Figure 1).[5d,6] A significant increase in durability of the Re(pyNHC-aryl)$(CO)_3$Br catalyst is also observed relative to the benchmark when an electron deficient aryl group was evaluated. However, only the inductively withdrawn *para*-CF_3-phenyl group was previously examined as an electron withdrawing group on the NHC ligand in the PCO_2RR. The effects of additional inductive electron withdrawing groups along with resonance electron withdrawing groups on the aryl ring has yet to be examined with this ligand design in the PCO_2RR.

[a] *H. Shirley,[+] Dr. T. M. Sexton,[+] Dr. N. P. Liyanage, M. A. Perkins, S. A. Autry, Dr. L. E. McNamara, Prof. N. I. Hammer, Prof. G. S. Tschumper, Prof. J. H. Delcamp*
Department of Chemistry and Biochemistry
University of Mississippi
322 Coulter Hall, University, MS 38677–1848 (USA)
E-mail: delcamp@olemiss.edu
tschumpr@olemiss.edu
[b] *Prof. S. R. Parkin*
Department of Chemistry
University of Kentucky
125 Chemistry/Physics Building, Lexington, KY 40506–0055 (USA)
[+] *These authors contributed equally to this work.*
[**] *NHC = N-heterocyclic carbene.*
Supporting information for this article is available on the WWW under https://doi.org/10.1002/cptc.202000296
Special Collection An invited contribution to a Special Collection on Photocatalytic CO_2 Reduction

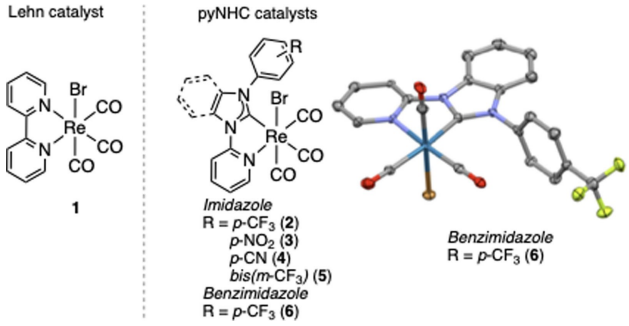

Figure 1. Structures of the first reported rhenium photocatalyst (**1**) for the PCO_2RR and the Re(PyNHC-aryl)$(CO)_3$Br photocatalysts studied in this work with varied electron withdrawing aryl-ring substituents (**2**–**5**) and extended π-conjugation at the NHC ring (**6**). The crystal structure of **6** is shown on the right.

A series of electron withdrawing aryl substituents were selected for comparison to known CF_3 substituted catalyst **2** (Figure 1).[5d] As π-electron withdrawing groups via resonance, nitro (**3**) and cyano (**4**) were targeted to compare resonance electron withdrawing group effects with the inductively withdrawing group effects of **2**. The bis-CF_3 substituted catalyst (**5**) was selected to evaluate the role of increasing the number of inductive electron withdrawing groups on catalyst properties. Additionally, an increase in conjugation at the imidazole portion of the ligand was probed with benzimidazole **6**. Since the addition of electron withdrawing groups provides increased reactivity relative to donor groups or hydrogen, we reasoned that if the electron withdrawing group role is to lower the energy of the first reduction of the catalyst then the extension of the π-system may further aid in this process. Herein, the catalyst properties are analyzed via absorption spectroscopy, emission spectroscopy, cyclic voltammetry, photocatalytic performance studies, computational analysis, excited-state lifetime studies, and emission quenching.

2. Results and Discussion

Complexes **2**–**5** have been previously reported, and complex **6** was prepared as described in the experimental section.[5d]

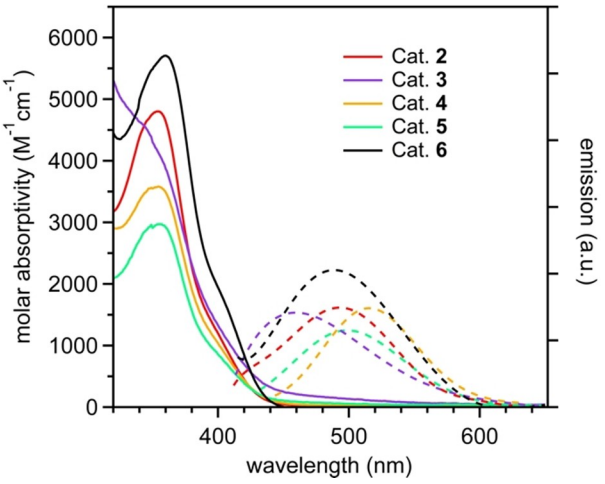

Figure 2. UV-Vis absorption (solid lines) and emission (dashed lines) spectra of catalysts **2**–**6**. All data was collected in acetonitrile and the emission is normalized to the height of the low energy shoulder of the absorption curve.

Complex **6** was fully characterized, including via crystallography, with details reported in the experimental section and in the supplementary information (Figures 1, S1–S10, S16–S18 and Tables S6–S11). The absorption data shows that nearly all the complexes (**2**–**6**) absorb light in the visible region with similar absorption curve onsets (λ_{onset}) of ~440 nm (Figure 2, Table 1). However, it should be noted that yellow complex **3** undergoes slight decomposition in solution to give a slowly forming green solution; however, in the solid state the complex seems stable. The observable decomposition indicates that the absorption curve features should be interpreted with caution despite it being freshly prepared and immediately subjected to measurements. Complexes **2**, **4**, and **5** all have absorption maxima (λ_{max}) shoulders estimated within ~1 nm, which indicates little influence of the aryl substituent on the photoexcitation energy needed to promote electrons to higher energy states regardless of the type of withdrawing substituent appended (Table 1). Complex **6** illustrates that extending conjugation leads to a noticeable change in the absorption curve with a red shifting of the λ_{max} value (Figure 2). Both aryl substituents and the extended conjugation had a significant effect on the molar absorptivity (ε) at λ_{max} following the trend: **6** ($\varepsilon = 5{,}800\ M^{-1}cm^{-1}$) > **2** ($\varepsilon = 4{,}800\ M^{-1}cm^{-1}$) > **4** ($\varepsilon = 3{,}600\ M^{-1}cm^{-1}$) > **5** ($\varepsilon = 3{,}000\ M^{-1}cm^{-1}$). Thus, the energy of the singlet metal-to-ligand charge transfer ($MLCT^1$) is not significantly affected by the ligand changes, while the intensity of the transition is tunable.

Emission measurements were significantly impacted by the type of withdrawing group on the aryl ring (Figure 2). The three CF_3 substituent complexes (**2**, **5**, and **6**) show relatively similar emission curve maxima (~495 nm). However, a significant effect is observed on the emission curve maximum energy when **2** is compared to **4** (a 20 nm or 0.12 eV shift in energy). The shift from the resonance electron withdrawing CN group suggests the aryl group substituent plays a significant role in controlling the excited-state energy level arrived at after intersystem crossing (ISC) to the $MLCT^3$ state. The nitro substituted complex **3** shows the highest emission maximum energy at 450 nm with a blue shift relative to the CF_3 substituted complexes, suggesting a relatively higher energy $MLCT^3$ state is arrived at after ISC. The $MLCT^3$-ground state energy gap ($E_{(MLCT\text{-}GS)}$) was estimated from the onset of emission for each catalyst on the high energy side to give the following trend: **2** = **3** > **6** > **5** > **4** ranging from 2.97 eV to 2.82 eV. This

Table 1. Photochemical and electrochemical data measured in acetonitrile.

Cat.	λ_{abs}^{max} [nm] peak (sh)[a]	ε [$M^{-1}cm^{-1}$] peak (sh)[a]	λ_{em}^{max} [nm]	τ [ns]	$E_{(MLCT\text{-}GS)}$ [eV][b]	$E_{(S/S^{-})}$ [V][c]	$E_{(S^*/S^{-})}$ [V][d]
2	356 (400)	4800 (1200)	496	4.3	2.97	−1.90	1.07
3	350 (400)	4800 (1400)	450	1.9	2.97	−1.90	1.07
4	357 (380)	3600 (1200)	520	4.3	2.82	−1.94	0.88
5	356 (400)	3000 (1000)	503	4.8	2.87	−1.94	0.93
6	360 (405)	5800 (2200)	494	6.9	2.94	−1.91	1.03

[a] "sh" indicates shoulder. [b] $E_{(MLCT\text{-}GS)}$ is estimated from the onset of the emission curve on the high energy side. [c] Measured via CV and reported versus ferrocenium/ferrocene under N_2. [d] Excited state reduction potential was calculated using the following equation: $E_{(S^*/S^{-})} = E_{(MLCT\text{-}GS)} + E_{(S/S^{-})}$.

observation shows that the ligand substituents can be used to tune the $E_{(MLCT\text{-}GS)}$ over a 150 meV range.

The reduction potential energy ($E_{(S/S-)}$) value of each catalyst was evaluated by cyclic voltammetry (CV) to ensure that each catalyst has sufficient free energy to reduce CO_2 by two electrons to CO (the E° value is believed to be between −0.9 V and −0.12 V versus Fc^+/Fc depending on the strongest acid generated under the photocatalytic conditions used below).[7] The CVs for catalysts **2**–**5** have been previously reported[5c] and catalyst **6** is shown in the SI (Figure S1). The first reduction potential of the catalysts (Figure 3) varied minimally from −1.90 V to −1.94 V between each of the catalysts. Compared to the bipyridyl benchmark catalyst **1**, the first reduction potentials of the NHC-based catalysts are shifted to more negative potentials by ~300 to 340 mV. Given the stronger electron donation strength of the NHC ligand relative to pyridine, this shift in potentials to more negative values is expected. Importantly, the NHC-based catalysts all have ample driving force for CO_2 reduction at the first reduction potential by at least 1.0 V even taking the reduction potential of CO_2 at the most negative estimated value.[5d]

A current increase is observed at both reduction peaks associated with catalyst **6**, similar to that previously reported for **2**–**5**, when the N_2 atmosphere is exchanged with a CO_2 atmosphere.[5c–d] The current peak height under CO_2 (i_{CO2}) was found to be 2.2 times higher than the current peak height under N_2 (i_{N2}) for catalyst **6** at the first reduction wave and 2.4 times higher at the second reduction wave. Interestingly, these complexes show increased current at the first reduction wave under CO_2. This is a property that has been observed by several NHC complexes during the electrocatalytic CO_2RR in the literature[8] and is hypothesized to be due to the second reduction occurring after association to CO_2 and being less thermodynamically demanding than the first reduction prior to CO_2 association to the catalyst.[9]

The energetic position of the excited-state reduction potentials ($E_{(S^*/S-)}$) of the catalysts are important to evaluate when considering possible sacrificial electron donor (SED) materials to drive the PCO_2RR. The $E_{(S^*/S-)}$ values were estimated to be 0.88 V to 1.07 V from the equation $E_{(S^*/S-)} = E_{(MLCT\text{-}GS)} + E_{(S/S-)}$. These values are all significantly more positive than the ground-state oxidation potential of either 1,3-dimethy-l-2-phenyl-2,3-dihydro-1H-benzo[d]imidazole (BIH; −0.10 V) or triethylamine (TEA; 0.42 V), indicating either reagent could transfer an electron to the photoexcited catalysts in the $MLCT^3$ state with favorable thermodynamics. Having found suitable thermodynamics for the reduction of CO_2 with a reduced catalyst, suitable thermodynamics for the electron transfer from a SED to the photoexcited catalyst, and an increased current response under CO_2, photocatalytic studies were next undertaken.

A solar simulated 150 W Xe lamp with an AM1.5G filter was used to drive the photocatalytic reactions. The intensity of the light was held constant in all photocatalytic experiments and BIH with TEA was used as the sacrificial electron source. CO formation was monitored by gas chromatography and no appreciable H_2 (by GC) or HCO_2^- (by ^1H NMR) was observed. Figure 4 shows the PCO_2RR results as turnover number (TON), in moles of CO per mole of catalyst, versus time plots to assess both catalyst durability (maximum TON) and initial rates (turnover frequency, TOF) from the slopes between early time points. The catalysts with resonance electron withdrawing groups (NO_2 and CN on catalysts **3** and **4**, respectively) have substantially lower TON and TOF values than the catalysts with inductively withdrawn CF_3 groups. The first data points for catalysts **2**, **5**, and **6** at 20 minutes are closely grouped near 15 TON. This shows these catalysts have similar TOF values; however, the durability of the catalysts varies significantly in the following order of TON values: **2** > **6** > **5**. Thus, the use of two CF_3 groups or a π-extended ligand system at the NHC ring leads to faster decomposition. All catalysts ceased CO production after 2 hours of irradiation.

All of the photocatalysts have ample driving force for CO_2 reduction and electron transfer from BIH after photoexcitation. If the excited state lifetime is relatively long-lived, the catalyst has more time to undergo electron transfer from the SED and

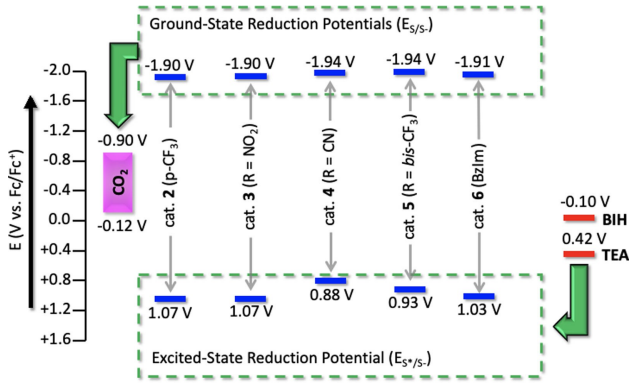

Figure 3. Energetic diagram of the ground-state ($E_{(S/S-)}$) and excited-state ($E_{(S^*/S-)}$) reduction potentials for catalysts **2**–**6**. An estimated reduction potential range for CO_2 and the oxidation potential of two SEDs is also shown.

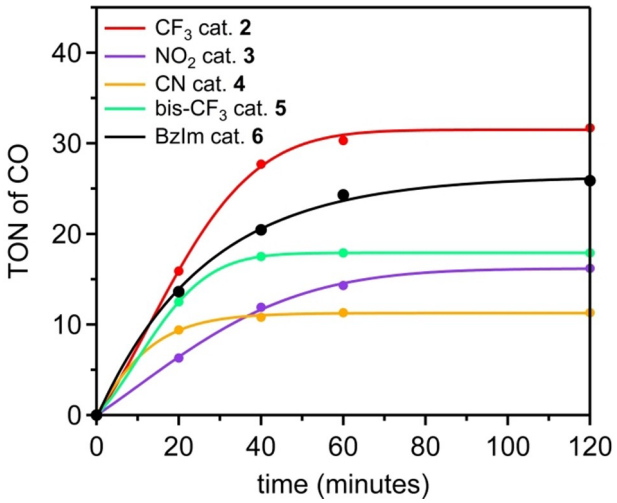

Figure 4. Turnover number versus time plot for **2**–**6** during the PCO_2RR. Photocatalysis reaction run under CO_2 in 2 mL of MeCN with 0.1 mM catalyst, 0.02 mmol BIH, and 0.72 mmol TEA.

continue along the catalytic cycle toward CO production. Thus, photophysical kinetic measurements and computational studies were undertaken to better understand the differences in performance in the PCO_2RR. The excited state lifetimes were measured by time-correlated single photon counting (TCSPC) via emission spectroscopy. All exponential decays were fit to a double exponential with the curves showing the catalyst varying the amount of slow and fast decay components present (Figure S21). The excited-state lifetimes of the NHC-based catalysts in this series are all short-lived (~2–7 ns) compared to the bipyridyl benchmark catalyst **1** (50 ns) (Table 1, Figure S21). When comparing the NHC catalysts **2** and **6**, the extended π-conjugated benzimidazole based complex had a longer lifetime (6.9 ns versus 4.3 ns). The shortest lifetime was observed with the resonance electron withdrawing NO_2 group on the aryl ring at 1.9 ns. The correlation of these values to catalyst reactivity is further discussed below.

The highest performing catalyst (**2**), the lowest performing catalyst (**3**), and the second highest performing catalyst (**6**) were analyzed computationally via density functional theory (DFT) with the M06-2X[10] and PBE0[10b,11] functionals and implicit MeCN solvation (see experimental section for a description of the computational approach and how the rhenium atom was treated). The M06-2X and PBE0 functionals have been successfully employed elsewhere to characterize the structures and ligand dissociation energies of transition metal complexes.[8a,10b] In addition, time dependant DFT (TDDFT) computations with both functionals have been shown to reliably reproduce experimental UV-Vis spectral features in combination with an appropriate implicit solvent model, specifically PBE0 with the closely related $Re(bpy)(CO)_3(Cl)$ complex and M06-2X with polycyclic organic dyes.[10b,12] Initially the geometries of the catalysts were optimized via DFT, and then TDDFT was used to access vertical transition energies and the orbitals involved in the S_0 to S_1 transition and the S_0 to S_2 transition. Catalyst **6** shows a reasonably high oscillator strength for the S_0 to S_1 transition (0.023 for M06-2X, 0.011 for PBE0) with a stronger S_0 to S_2 transition observed at 0.069 for M06-2X and 0.075 for PBE0 (Table S3). When combined with an implicit solvent model, both M06-2X and PBE0 overestimate the vertical excitation energy value relative to the experimentally observed value for the S_0 to S_1 transition in solution (3.79 eV for M062X, 3.21 eV for PBE0, and 3.06 eV experimentally in MeCN). These differences appear to be largely systematic, suggesting that meaningful correlations between the experimentally measured properties and the computed theoretical values can be established. With both levels of theory, the S_0 to S_1 transition near the region of the ground state optimized structure is dominated ($\geq$90%) by an electronic excitation from the highest occupied molecular orbital (HOMO) to the lowest unoccupied molecular orbital (LUMO) (Table S3). The HOMO is primarily located on the metal center with both levels of theory (Figure 5); however, the contribution from the benzimidazole ligand is slightly more pronounced with the M06-2X functional. In both cases, the LUMO is predominantly located on the pyridyl ligand which suggests these catalysts are undergoing MLCT transitions upon photoexcitation as the lowest energy

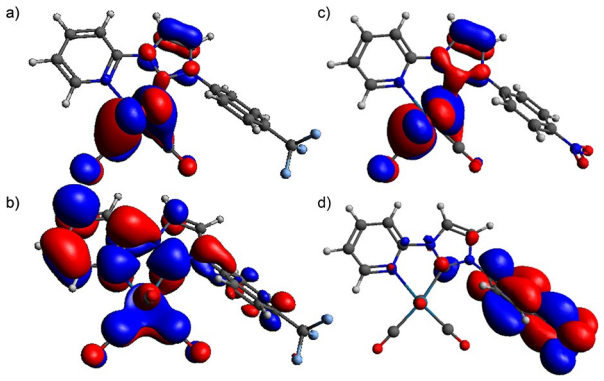

Figure 5. Orbital images obtained using the M06-2X functional for catalyst **2** HOMO (a), catalyst **2** LUMO (b), catalyst **3** HOMO (c), and catalyst **3** LUMO (d).

transition. Comparatively, catalyst **2** shows a shift, relative to catalyst **6**, of the lowest energy vertical transition to higher energy at 3.85 eV with M06-2X or 3.23 eV with PBE0 which are 60 meV and 20 meV shifts, respectively (Table S1). Experimentally, a shift toward higher energy is also observed to 3.10 eV which is about a 40 meV shift relative to the π-extended catalyst **6**. These results show that the benzimidazole π-extension introduction strategy does impart a modest shift of the absorption spectrum maxima (and shoulder feature) toward absorbing deeper into the visible region experimentally (about a 5 nm red-shift of curve features) which agrees with computational results. Notably, the absorption curve onsets experimentally are near identical between catalyst **2** and catalyst **6**. Computationally, the vertical transition oscillator strength is reduced for catalyst **2** (M06-2X = 0.015, PBE0 = 0.008) relative to catalyst **6** for both levels of theory. This is consistent with the experimental observation that catalyst **2** has a lower molar absorptivity than catalyst **6**. Again, both levels of theory predict the lowest energy vertical transition to be primarily HOMO to LUMO ($\geq$86%), which appears to be primarily MLCT based (Figures 5 and S13).

Catalyst **3** is the only one in the series for which pronounced differences are observed between the M06-2X and PBE0 oscillator strengths of the vertical transitions. For catalysts **2** and **6**, the second lowest energy vertical transition was approximately three times larger than the first vertical transition with respect to oscillator strengths. Catalyst **3** showed the same behavior at the M06-2X level of theory; however, for PBE0 the oscillator strength of the second vertical transition was about half the strength of the first vertical transition (Table S2). Experimentally, in the lower energy region from 350 nm to 450 nm the absorption curve features of **3** do not vary dramatically relative to **2** in terms of shape or molar absorptivity as M06-2X predicts (Figures 2 and S15). Additionally, the shift in vertical transition energy when changing the CF_3 substituent of **2** to a nitro substituent for **3** is predicted to be modest for M06-2X at 30 meV but dramatic with PBE0 at 360 meV. Experimentally, there is no significant change in the lowest energy absorption feature when **2** and **3** are compared, which is consistent with the M06-2X prediction. Thus, while

PBE0 has better agreement with the magnitudes of the experimental vertical transition energies when referencing the absorption maxima, M06-2X has a dramatically better agreement with the experimentally observed electronic structure with reference to the relative transition intensities for the first two transitions of catalyst **3** and a better agreement with experiment for the relative absorption spectrum shifts seen between catalyst derivatives. Interestingly, M06-2X predicts the lowest energy vertical transition is predominately made of the HOMO to LUMO + 1 transition (66%) with a 22% contribution of the HOMO to LUMO transition (Figure S12, Table S2). The HOMO orbital is similarly positioned for catalyst **3** to that observed for **2** and **6**. However, the LUMO is predicted to be almost entirely on the aryl-NO_2 ring. This differs dramatically from **2** and **6**, which shows the LUMO on the pyridyl ring. The LUMO + 1 of **3** is analogously positioned similar to the LUMO of **2** and **6**. This indicates that the nitro group has uniquely shifted the aryl ring to becoming a better acceptor upon excitation than the pyridyl ring for the MLCT event. This may in part explain the poor performance of **3** photocatalytically, since the strongly electron accepting aryl-nitro ring has very poor orbital overlap with the Re metal center which correlates to a low TOF experimentally. This leads to the conclusion that the aryl ring substituent can be used to modulate reactivity through the introduction of electron withdrawing groups to accelerate the PCO_2RR; however, if the aryl ring becomes more electron deficient than the pyridyl ring, catalysis is slowed. While exact agreement is neither expected nor observed between absolute numbers from theory and experiment in these studies, M06-2X seems to provide better correlation with both molar absorptivity trends, catalyst absorption spectrum shift trends, and photocatalytic results.

We have previously noted that upon reduction, the aryl ring plays a significant role in electron delocalization following a geometry reorganization that planarizes the aryl and NHC π-systems.[5d] To examine if this behavior persists upon π-extending the NHC ligand and upon introduction of a strong resonance electron withdrawing group, the one electron reduced singly occupied molecular orbital (SOMO) was analyzed after geometry optimization at the M06-2X level of theory for **2**, **3**, and **6** (Figure 6). Interestingly, **2** and **6** show delocalization of the SOMO orbital across the metal center, pyridyl ring, NHC ring, and aryl ring. The steric repulsion of the hydrogens on the benzimidazole ring and the aryl ring does limit the extent of planarity that the aryl ring can reach with respect to the pyridyl/NHC rings; however, a significant amount of orbital contribution remains on the aryl ring. The benzene ring on the benzimidazole group has minimal involvement with the SOMO. Thus, the benzimidazole group has modestly increased light absorption properties (red-shifted spectrum, increased molar absorptivity), but has lowered the involvement of the aryl ring in the singly reduced state. Catalyst **3** deviates dramatically in SOMO orbital position with the orbital being almost exclusively on the nitro substituted aryl ring with no involvement of the rhenium atom and trace presence on the pyridyl and NHC rings. This suggests the highest energy electron on the one-electron reduction complex is effectively

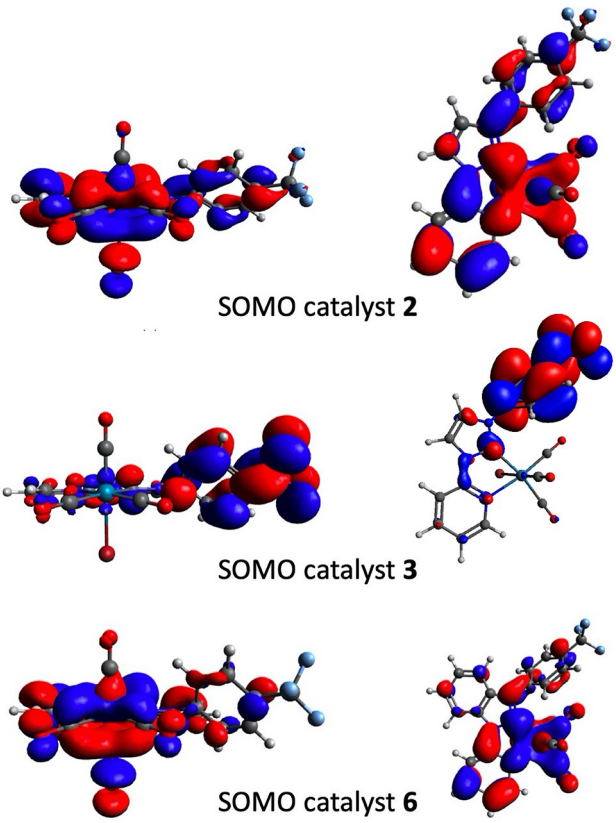

Figure 6. SOMO orbitals of the one-electron-reduced catalysts obtained using the M06-2X functional.

being trapped away from the metal center, which could limit delivery of the electron to CO_2 from the rhenium center and be related to the poor catalytic performance of **3** which has been suggested by prior catalytic studies as well.[2i–j]

The dissociation energies of the bromine anion from the singly reduced catalysts were probed computationally at both the PBE0 and M06-2X levels of theory (Table 2). The dissociation energies of all catalysts except **3** were found to be in the 1.8–4.8 kcal/mol range for both levels of theory. Compared to the other catalysts, catalyst **3** shows a dramatically larger dissociation energy of 20.2 and 25.8 kcal/mol with PBE0 and M06-2X, respectively. This is likely related to the SOMO orbital position lacking electron density at the Re metal center and thus disfavoring Br^- loss. This almost certainly impedes catalysis since a Br^- group must be dissociated in order to open a reactive coordination site for CO_2. The trend for dissociation

Table 2. Computed energy of dissociation (D_0) in [kcal mol^{-1}] of the Br ligand with each catalyst under PBE0 and M06-2X functionals in solvent. (See Tables S4 and S5 for full D_0 results).

Catalyst	PBE0	M06-2X
2	2.1	3.4
3	20.2	25.8
4	3.2	4.8
5	2.5	3.8
6	1.8	2.7

energies is the same for both levels of theory, with the order of least to most energy required for Br^- dissociation being **6** < **2** < **5** < **4** ≪ **3**. Thus, the π-extended derivative leads to the most easily dissociated Br^- group, possibly due to the SOMO being slightly more localized on the Re metal center of **6** relative to **2**. Next, the two catalysts with inductively electron withdrawing groups on the aryl ring (**2** and **5**) show easier Br^- dissociation than those with resonance withdrawing groups (**4** and **3**). The energy required for dissociation appears to be directly related to the SOMO orbital position, with the cyano substituted catalyst **4** showing a similar involvement of the SOMO on the aryl ring relative to **5** (Figure S14).

Both lifetime and dissociation energy of the Br^- from the singly reduced catalysts has some correlation with the TOF values observed. Fortuitously, the TOF values are nearly linear in increasing increments across the catalyst series from **3** < **4** < **5** < **6** < **2** with an R^2 value of 0.96 (Figure 7). The near linear increase in TOF across the series is arbitrarily found but allows for simple correlative comparisons to other observables such as excited state lifetimes and Br^- dissociation energy. Each of these parameters were normalized and plotted for comparison of trends with TOF changes. The dissociation energy was plotted as an inverse value since lower dissociation energies would be predicted to correlate with higher TOF rates. While there is not necessarily a relation between these parameters given the complex number of steps in the PCO_2RR involving catalyst excitation, electron transfers, and the chemical bond breaking/forming events required to reduce CO_2 to CO, it is interesting that significant correlations exist and can perhaps be used as predictive measures for improving catalyst performance in the PCO_2RR. Both excited state lifetime and Br^- dissociation energies track well with the TOF values across all of the catalysts with the exception of **2**, which has a faster TOF than would be expected based on the shorter excited-state lifetime and higher barrier for Br^- dissociation for **2** relative to **6**. The suggested correlation of TOF, excited-state lifetime, and Br^- dissociation was predictive across the catalysts; however, additional important parameters are likely needed for a fully predictive model, since catalyst **2** is more weakly correlated to the trends observed than the other four catalysts between TOF and lifetime.

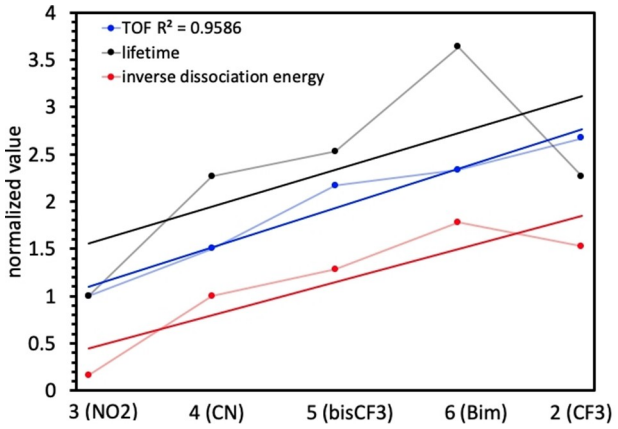

Figure 7. Correlation of TOF to lifetime and dissociation energies which are all normalized to the lowest performing catalyst except for the inverse dissociation energy data points which are normalized to the second lowest performing catalyst due to the large energy difference of the nitro functionalized catalyst relative to the rest of the series. Linear trendlines are added as dark lines and the lighter colored lines are used to connect data points in the series. The linear fit line for the lifetime trendline has an R^2 value of 0.43, and the dissociation trendline has an R^2 value of 0.72. Notably, in the absence of catalyst **2**, R^2 values of 0.95 and 0.96 are obtained, respectively. See SI Figure S22 for a plot with added electrochemical TOF values.

Stern-Volmer quenching studies were undertaken with **2** and **6** with varied BIH concentrations to probe the catalysts for differences that might better explain the higher performance of **2** (Figure 8). Both catalysts show linear quenching rates for initial emission intensity (I_0)/quenched emission intensity (I) versus concentration of BIH over a range of 1 mM to 25 mM concentrations, indicating diffusion-controlled kinetics. The Stern-Volmer constants for both catalysts were low at 0.36 for catalyst **2** and 0.15 for catalyst **6** (Figures 8, S19–S20). The quenching rate of photoexcited **2** is about two-fold higher than the quenching rate of **6** with BIH, despite the catalysts having nearly identical excited-state reduction potentials. While the origin of this difference is non-obvious from these studies, this result shows that the faster quenching of **2** is correlated with the faster TOF value of **2** relative to **6**, despite **6** having a longer excited-state lifetime in solution. Notably, higher quenching rates are not necessarily correlated to length of excited-state lifetimes.[13]

3. Conclusion

A new benzimidazole-based Re(pyridyl-NHC) catalyst was synthesized, evaluated in the PCO_2RR, and characterized using crystallographic, photophysical, computational, and electrochemical methods. This complex was compared to a series of 4 known Re(pyridyl-NHC) complexes with three of these complexes being studied in the PCO_2RR for the first time. The series of pyridyl-NHC catalysts varies electron withdrawing groups on the aryl group linked to the NHC ring and the extent of π-conjugation at the NHC ring. Notably, all catalysts act as direct photocatalysts for the CO_2 reduction reaction in the presence of an SED with varying TOF and TON values. Inductively

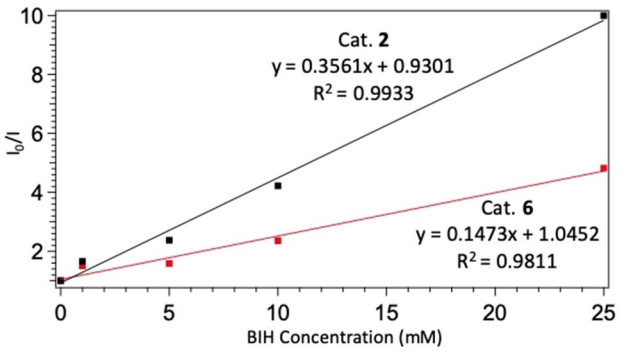

Figure 8. Stern-Volmer quenching plots of **2** and **6** with BIH.

electron withdrawing substituents were found to give catalysts that have faster TOF values relative to the π-electron withdrawing groups via resonance. This observation was computationally analyzed with findings showing that π-electron withdrawing groups via resonance move electron density in the SOMO of the singly reduced complex further from the Re center, leading to higher energy barriers to Br^- ligand dissociation from the complexes. Since a catalyst reactive site must be opened for CO_2 coordination, a higher energetic barrier to anionic ligand dissociation is likely related to slow catalysis. Additionally, catalyst TOF values in the PCO_2RR were correlated to excited-state lifetimes and inversely correlated to Br^- dissociation energies. Only one of the 5 complexes studied deviated from this correlation which was found to undergo significantly faster excited state quenching with an SED despite a shorter excited state lifetime than the second highest TOF value catalyst studied. Importantly, these studies show a "sweet spot" in terms of electron withdrawing groups on the ligand with respect to catalyst performance. Initial reports with this ligand scaffold show electron withdrawing groups enhancing catalyst performance. However, this report shows that this approach is limited due to electron withdrawing group strength increasingly removing electron density from near the Re center to the aryl ring. This leads to slower dissociation of the Br^- group and slower catalysis with exceptionally strong electron withdrawing groups.

Experimental Section

Experimental General Information

All commercially obtained reagents were used as received. Unless otherwise noted, all the reactions were conducted under a N_2 atmosphere. Thin-layer chromatography (TLC) was conducted with Sigma T-6145 pre-coated TLC silica gel 60 F_{254} polyester sheets and visualized with 254 nm light. Flash column chromatography was performed with SilicaFlash P60, 40–63 μm (230-400 mesh). ^{1}H NMR spectra were recorded on a Bruker Avance-400 (400 MHz) spectrometer and reported in ppm using residual non-deuterated solvent as an internal standard (CD_3CN at 1.94 ppm). Data reported as: s = singlet, d = doublet, t = triplet, q = quartet, p = pentet, m = multiplet, ap = apparent; coupling constants in Hz. FT-IR samples were run on a Bruker Alpha ATIR spectrometer. UV-Vis spectra were collected on a Cary 5000 spectrometer. Emission spectra were collected using a PerkinElmer LS55 Fluorescence Spectrometer. Samples for emission studies were degassed with N_2 prior to collecting spectra in acetonitrile. Cyclic voltammetry was performed using a CH Instruments potentiostat (CHI-600E) with a glassy-carbon electrode as the working electrode, platinum as the counter electrode, and silver wire as the pseudo-reference electrode with ferrocene as an internal reference. 0.1 M *n*-Bu_4NPF_6 was used as the supporting electrolyte and all the measurements were taken in acetonitrile. 1.0 mM catalyst concentration was used in each experiment. Before each measurements the electrolyte solution was degassed with N_2 or CO_2 (~15 min). To avoid changes in concentration during degassing, pure acetonitrile was first added to the electrolyte solution and the solution was degassed until the final volume was reduced to the original electrolyte volume. CV measurements were taken at a scan rate of 100 mV/s^{-1}, and the sweep width window was set to ~100 mV past the second reduction potential for each catalyst. A 150 W Sciencetech SF-150 C small collimated beam solar simulator equipped with an AM1.5 G filter was used as the light source for the photocatalytic experiments. Head space analysis was performed using gas tight valved syringes to extract the sample, and analysis of the same was performed with a custom Agilent 7890B gas chromatography instrument equipped with an Agilent PorapakQ 6ft, 1/8 O.D. column. Quantification of CO and CH_4 were made using an FID detector, while H_2 was quantified using a TCD detector. No significant amounts of CH_4, H_2, or HCO_2^- (by NMR) were observed. All GC calibration standards were purchased from BuyCalGas.com. Complexes **2**–**5** are previously reported although not evaluated in the PCO_2RR.[5c–d] 1,3-dimethy-l-2-phenyl-2,3-dihydro-1H-benzo[d] imidazole (BIH) was prepared as previously reported.[5d]

Synthesis (see Figure 9 for the letters used to reference intermediates): 1-(4-(trifluoromethyl)phenyl)-1H-benzo[d] imidazole (C)

A flame-dried flask equipped with a stir bar was charged with benzimidazole (**A**) (1.77 g, 15.0 mmol), 1-bromo-4-triflurometh-ylbenzene (**B**) (2.38 g, 10.7 mmol), and dry, degassed DMF (11 mL). Solid CuI (0.41 g, 2.14 mmol) and K_3PO_4 (4.54 g, 21.4 mmol) were added to the flask together in one portion. The reaction mixture was then heated to 130 °C under N_2 with stirring, and monitored by ^{1}H NMR spectroscopy. After 20 h, the reaction mixture was cooled to room temperature and diluted with Et_2O (100 mL), washed 3 times with H_2O (200 mL), and dried with $MgSO_4$. Once concentrated, the crude product mixture was passed through a short plug of silica using first with 50% hexanes:50% Et_2O eluent, then 100% EtOAc to elute the product. Product fractions were concentrated to give a white microcrystalline solid (2.51 g, 64%). IR (neat, cm^{-1}): 3293, 2928, 2857, 1629, 1530, 1039. ^{1}H NMR (400 MHz, CD_3CN): δ 8.29 (s, 1H), 7.93 (d, J = 8.4 Hz, 2H), 7.82 (d, J = 8.0 Hz, 2H), 7.80 (d, J = 8.4 Hz, 1H), 7.66 (d, J = 8.0 Hz, 1H), 7.37 (ap p, J = 6.8 Hz, 2H) ppm. ^{13}C NMR (100 MHz, CD_3CN): δ 144.9, 143.3, 140.3, 133.7, 129.3 (q, J = 32.5 Hz), 127.72 (q, J = 3.8 Hz), 124.8, 124.5, 123.3, 122.1 (q, J = 269.0 Hz), 111.3 ppm. One signal may not be unique. The signal at 124.8 ppm could be overlapping signals. ^{19}F NMR ((376 MHz, CD_3CN): δ −62.9 ppm. ESI HRMS calc'd for $[M+H]^+$ $C_{14}H_{10}F_3N_2$ = 263.0796; found 263.0775.

3-(pyridin-2-yl)-1-(4-(trifluoromethyl)phenyl)-1H-benzo[d] imidazol-3-ium bromide (E)

A sealable tube was charged with 1-(4-trifluoromethylphenyl)-1H-benzo[d]imidazole (**C**) (0.60 g, 2.35 mmol) and 2-bromopyridine (**D**) (0.41 mL, 0.72 g, 4.70 mmol), heated to 175 °C under N_2, and monitored by ^{1}H NMR spectroscopy. After 3 days, the reaction

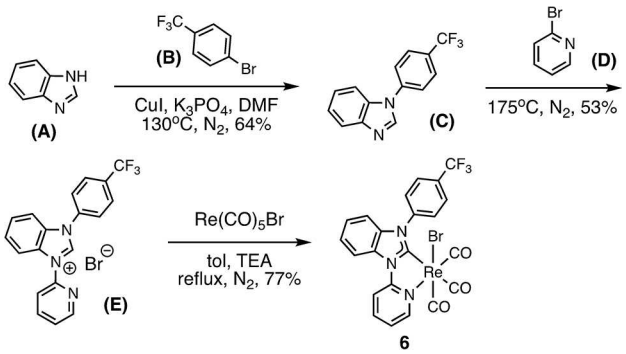

Figure 9. Synthetic route for catalyst **6**.

mixture was cooled to room temperature, at which time a precipitate formed. The contents of the tube were dissolved in dichloromethane, and the product precipitated using Et_2O as a pale brown microcrystalline solid (0.52 g, 53%). IR (neat, cm^{-1}): 3293, 2928, 2857, 1629, 1530, 933. ^1H NMR (400 MHz, CD_3CN): δ 8.79 (d, $J=4.8$ Hz, 1H), 8.55–8.40 (m, 1H), 8.26–7.90 (m, 7H), 7.85–7.75 (m, 3H), 7.75–7.60 (m, 1H) ppm. ^{13}C NMR (100 MHz, CD_3CN): δ 150.4, 147.7, 141.4, 141.2, 136.5, 131.7 (q, $J=186.5$ Hz), 129.1, 129.0, 128.3 (q, $J=3.8$ Hz), 127.2, 126.3, 116.9, 114.3 ppm. The two bond C–F coupling is not obvious from the spectrum, although it is possibly the signals at approximately 129 ppm. It is presumed some of the signals are overlapping. ^{19}F NMR (376 MHz, CD_3CN): δ −63.3 ppm. ESI HRMS calc'd for $[M-Br]^+$ $C_{19}H_{13}N_3F_3=340.1062$; found 340.0987.

fac-(3-(4-trifluoromethylphenyl)-1-(2′-pyridyl) benzimidazolin-2-ylidene) tricarbonylbromorhenium(I) (6)

A flame dried flask equipped with a stir bar and reflux condenser were charged with 3-(pyridin-2-yl)-1-(4-(trifluoromethyl)phenyl)-1H-benzo[d]imidazol-3-ium bromide (**E**) (0.10 g, 0.27 mmol), $Re(CO)_5Br$ (0.11 g, 0.27 mmol), dry, degassed toluene (4.55 mL), and TEA (0.38 mL, 0.27 g, 2.7 mmol). The reaction mixture was warmed to reflux under N_2 with stirring in the dark, and monitored by ^1H NMR spectroscopy. After 4 days, the reaction mixture was concentrated on a rotary evaporator, and the crude product purified by SiO_2 column chromatography using 10% EtOAc/CH_2Cl_2. Product fractions were concentrated to yield a pale-yellow solid (0.14 g, 77% yield). IR (neat, cm^{-1}): 3125, 2922, 2848, 2018, 1929, 1891, 1810, 1616, 1593, 1475, 1419, 1323, 779. ^1H NMR (400 MHz, CD_3CN): δ 8.99 (d, $J=6.8$ Hz, 1H), 8.46 (d, $J=8.8$ Hz, 1H), 8.35–8.20 (m, 2H), 8.06 (d, $J=8.4$ Hz, 2H), 7.80–7.60 (m, 2H), 7.41 (t, $J=8.0$ Hz, 1H), 7.31 (t, $J=8.1$ Hz, 1H), 7.25 (t, $J=6.7$ Hz, 1H), 7.07 (d, $J=8.1$ Hz, 1H) ppm. ^{13}C NMR (100 MHz, CD_3CN): δ 204.1, 197.8, 196.2, 188.5, 154.9, 154.5, 142.6, 141.1, 137.3, 132.4, 132.0, 131.4, 130.1, 129.6, 128.0 (q, $J=3.54$ Hz), 127.5, 126.4, 126.3, 124.1, 114.7, 113.4, 113.0 ppm. It is not apparent where the one and three bond C–F coupling is. It is presumed some of the signals are overlapping. ^{19}F NMR (376 MHz, CD_3CN): δ −63.2 ppm. ESI HRMS calc'd for $[M+Cs]^+$ $C_{22}H_{12}BrCsF_3N_3O_3Re=821.8626$; found 821.8635.

Single-crystal X-ray Diffraction

Crystals were formed by taking up the complex into MeCN, and subjecting the solution to a slow vapor diffusion of Et_2O to give the complex toward the top of the inner chamber. X-ray diffraction data were collected at 90.0(2) K on a Bruker D8 Venture kappa-axis diffractometer using MoKα X-rays. Raw data were integrated, scaled, merged and corrected for Lorentz-polarization effects using the APEX3 package.[14] Corrections for absorption were applied using SADABS.[15] The structure was solved by direct methods (SHELXT)[16] and refinement was carried out against F^2 by weighted full-matrix least-squares (SHELXL).[17] Hydrogen atoms were found in difference maps, but subsequently placed at calculated positions and refined using a riding model. Non-hydrogen atoms were refined with anisotropic displacement parameters. Structure quality was checked using published methods.[18] Atomic scattering factors were taken from the International Tables for Crystallography.[19] Crystal data and relevant details of the structure determinations for catalyst **6** are summarized in the SI, Table S6 and selected geometrical parameters are given in SI Tables S7–S11.

Photocatalysis general procedure

The photocatalysis procedure has been reported previously and was followed for these studies.[8a]

Computational Details

Full geometry optimizations and harmonic vibrational frequency computations were performed on the anionic and neutral species of catalysts **2**–**6** and their corresponding dissociation products using M06-2X[10] and PBE0.[11] An unrestricted spin reference was used for the open shell (doublet) species. The functionals were used in conjunction with Dunning and coworker's correlation consistent double-ζ basis set augmented with diffuse functions (aug-cc-pVDZ) and a relativistic pseudopotential for rhenium (aug-cc-pVDZ-PP),[20] both abbreviated as aDZ hereafter. After optimized structures were confirmed to be minima (i.e. had no imaginary frequencies), single-point computations were performed on those structures using the same functionals with the aug-cc-pVTZ basis set (aug-cc-pVTZ-PP for rhenium) to obtain electronic energies. Time-dependent DFT (TD-DFT) single-point computations[21] were carried out on the ground state optimized complexes using both M06-2X and PBE0 with the aDZ basis set in order to obtain vertical excitation energies[22] and oscillator strengths. For all computations, the effects of the acetonitrile solvent were incorporated by using the polarizable continuum model (PCM) with the default solvent parameters.[23] Electronic dissociation energies (D_e) were calculated by comparing electronic energies of the coordinated complex to the isolated ligand (Br^-) and remaining rhenium complex. Zero-point vibrational energy corrected D_e values (D_0) were obtained using the double-ζ unscaled harmonic vibrational frequencies and the triple-ζ electronic energies. D_0 values are reported for comparison with experimental values. All computations were performed using Gaussian 16 (Rev. C.01) with the ultrafine pruned numerical integration grid containing 99 radial shells and 590 angular points per shell.[24]

Stern-Volmer Quenching Studies

Emission spectra for the BIH quenching study were obtained using a Horiba QuantaMaster 8075-21 spectrofluorometer with a xenon lamp excitation source monochromated to 350 nm. Catalyst **2** and catalyst **6** solutions were prepared in acetonitrile at a concentration of 0.1 mM. BIH concentrations were also prepared in acetonitrile, and serial dilutions were performed from a stock solution. Spectra were measured under N_2 with degassed solvent.

Time-Correlated Single Photon Counting Studies

Emission lifetimes were obtained by exciting with a Picoquant LDH-P-C-405B 405 nm diode laser (fwhm < 100 ps) and detecting with a PDM series single photon avalanche diode (Micro Photon Devices, Bolzano, Italy). All solutions were N_2 degassed prior to obtaining data. All emission decay curves were fit with a double exponential decay function.

Acknowledgements

HS and JHD thank the National Science Foundation (NSF) for supporting this work with award 1800281. NL, LEM, SAA, NIH, and JHD thank NSF for award 1539035 under which initial data was collected. TMS, MAP, and GST acknowledge supported from the National Science Foundation (CHE-1338056 and CHE-1664998)

and also thank the Mississippi Center for Supercomputing Research (MCSR) for a generous allocation of time on their computational resources. The D8 Venture diffractometer was funded by the NSF (MRI CHE1625732 to SP).

Conflict of Interest

The authors declare no conflict of interest.

Keywords: carbene ligands · carbon dioxide · catalysis · density functional calculations · photocatalysis · rhenium

[1] a) M. Robert, *ACS Energy Lett.* **2016**, *1*, 281–282; b) M. Aresta, A. Dibenedetto, A. Angelini, *Chem. Rev.* **2014**, *114*, 1709–1742; c) M. Mikkelsen, M. Jørgensen, F. C. Krebs, *Energy Environ. Sci.* **2010**, *3*, 43–81; d) H. Ishida, C. Machan, M. Robert, N. Iwasawa, *Front. Chem.* **2020**, *8*; e) V. Artero, M. Fontecave, *Chem. Soc. Rev.* **2013**, *42*, 2338–2356; f) N. S. Lewis, D. G. Nocera, *Proc. Natl. Acad. Sci. USA* **2006**, *103*, 15729–15735.

[2] a) V. Kumaravel, J. Bartlett, S. C. Pillai, *ACS Energy Lett.* **2020**, *5*, 486–519; b) B. Zhang, L. Sun, *Chem. Soc. Rev.* **2019**, *48*, 2216–2264; c) N. I. Hammer, S. Sutton, J. Delcamp, J. D. Graham, in *Handbook of Climate Change Mitigation and Adaptation* (Eds.: W.-Y. Chen, T. Suzuki, M. Lackner), Springer International Publishing, Cham, **2017**, pp. 2709–2756; d) X. Liu, S. Inagaki, J. Gong, *Angew. Chem. Int. Ed.* **2016**, *55*, 14924–14950; *Angew. Chem.* **2016**, *128*, 15146–15174; e) C. D. Windle, E. Reisner, *Chimia* **2015**, *69*, 435–441; f) J. L. White, M. F. Baruch, J. E. Pander, Y. Hu, I. C. Fortmeyer, J. E. Park, T. Zhang, K. Liao, J. Gu, Y. Yan, T. W. Shaw, E. Abelev, A. B. Bocarsly, *Chem. Rev.* **2015**, *115*, 12888–12935; g) G. Sahara, O. Ishitani, *Inorg. Chem.* **2015**, *54*, 5096–5104; h) R. Reithmeier, C. Bruckmeier, B. Rieger, *Catalysts* **2012**, *2*, 544–571; i) P. Lang, C. Matlachowski, M. Schwalbe, *ChemistrySelect* **2017**, *2*, 4767–4773; j) B. Gholamkhass, H. Mametsuka, K. Koike, T. Tanabe, M. Furue, O. Ishitani, *Inorg. Chem.* **2005**, 44, 2326–2336.

[3] a) M. N. Hopkinson, C. Richter, M. Schedler, F. Glorius, *Nature* **2014**, *510*, 485–496; b) D. Morales-Morales, C. M. Jensen, in *The Chemistry of Pincer Compounds* (Eds.: D. Morales-Morales, C. M. Jensen), Elsevier Science B. V., Amsterdam, **2007**, p. xv.

[4] a) L. Suntrup, F. Stein, J. Klein, A. Wilting, F. G. L. Parlane, C. M. Brown, J. Fiedler, C. P. Berlinguette, I. Siewert, B. Sarkar, *Inorg. Chem.* **2020**, *59*, 4215–4227; b) E. S. Gauthier, L. Abella, N. Hellou, B. Darquié, E. Caytan, T. Roisnel, N. Vanthuyne, L. Favereau, M. Srebro-Hooper, J. A. G. Williams, J. Autschbach, J. Crassous, *Angew. Chem. Int. Ed.* **2020**, *59*, 8394–8400; c) T. P. Nicholls, L. K. Burt, P. V. Simpson, M. Massi, A. C. Bissember, *Dalton Trans.* **2019**, *48*, 12749–12754; d) P. V. Simpson, M. Falasca, M. Massi, *Chem. Commun.* **2018**, *54*, 12429–12438; e) T. Mukuta, P. V. Simpson, J. G. Vaughan, B. W. Skelton, S. Stagni, M. Massi, K. Koike, O. Ishitani, K. Onda, *Inorg. Chem.* **2017**, *56*, 3404–3413; f) P. V. Simpson, B. W. Skelton, P. Raiteri, M. Massi, *New J. Chem.* **2016**, *40*, 5797–5807; g) J. G. Vaughan, B. L. Reid, S. Ramchandani, P. J. Wright, S. Muzzioli, B. W. Skelton, P. Raiteri, D. H. Brown, S. Stagni, M. Massi, *Dalton Trans.* **2013**, *42*, 14100–14114; h) X.-W. Li, H.-Y. Li, G.-F. Wang, F. Chen, Y.-Z. Li, X.-T. Chen, Y.-X. Zheng, Z.-L. Xue, *Organometallics* **2012**, *31*, 3829–3835; i) A. Maurin, C.-O. Ng, L. Chen, T.-C. Lau, M. Robert, C.-C. Ko, *Dalton Trans.* **2016**, 45, 14524–24529.

[5] a) S. Gonell, E. A. Assaf, K. D. Duffee, C. K. Schauer, A. J. M. Miller, *J. Am. Chem. Soc.* **2020**, *142*, 8980–8999; b) S. Gonell, M. D. Massey, I. P. Moseley, C. K. Schauer, J. T. Muckerman, A. J. M. Miller, *J. Am. Chem. Soc.* **2019**, *141*, 6658–6671; c) N. P. Liyanage, H. A. Dulaney, A. J. Huckaba, J. W. Jurss, J. H. Delcamp, *Inorg. Chem.* **2016**, *55*, 6085–6094; d) A. J. Huckaba, E. A. Sharpe, J. H. Delcamp, *Inorg. Chem.* **2016**, *55*, 682–690.

[6] C. A. Carpenter, P. Brogdon, L. E. McNamara, G. S. Tschumper, N. I. Hammer, J. H. Delcamp, *Inorganics* **2018**, *6*, 22.

[7] R. R. Rodrigues, C. M. Boudreaux, E. T. Papish, J. H. Delcamp, *ACS Appl. Energy Mater.* **2019**, *2*, 37–46.

[8] a) H. Shirley, T. M. Sexton, N. P. Liyanage, C. Z. Palmer, L. E. McNamara, N. I. Hammer, G. S. Tschumper, J. H. Delcamp, *Eur. J. Inorg. Chem.* **2020**, *2020*, 1844–1851; b) S. Das, R. R. Rodrigues, R. W. Lamb, F. Qu, E. Reinheimer, C. M. Boudreaux, C. E. Webster, J. H. Delcamp, E. T. Papish, *Inorg. Chem.* **2019**, *58*, 8012–8020; c) C. M. Boudreaux, N. P. Liyanage, H. Shirley, S. Siek, D. L. Gerlach, F. Qu, J. H. Delcamp, E. T. Papish, *Chem. Commun.* **2017**, *53*, 11217–11220; d) C. J. Stanton, J. E. Vandezande, G. F. Majetich, H. F. Schaefer, J. Agarwal, *Inorg. Chem.* **2016**, *55*, 9509–9512; e) C. J. Stanton, C. W. Machan, J. E. Vandezande, T. Jin, G. F. Majetich, H. F. Schaefer, C. P. Kubiak, G. Li, J. Agarwal, *Inorg. Chem.* **2016**, *55*, 3136–3144; f) T. Jin, D. He, W. Li, C. J. Stanton, S. A. Pantovich, G. F. Majetich, H. F. Schaefer, J. Agarwal, D. Wang, G. Li, *Chem. Commun.* **2016**, *52*, 14258–14261; g) J. A. Therrien, M. O. Wolf, B. O. Patrick, *Inorg. Chem.* **2014**, *53*, 12962–12972; h) J. Agarwal, T. W. Shaw, C. J. Stanton, G. F. Majetich, A. B. Bocarsly, H. F. Schaefer, *Angew. Chem. Int. Ed.* **2014**, *53*, 5152–5155; *Angew. Chem.* **2014**, *126*, 5252–5255.

[9] H. Shirley, M. T. Figgins, C. M. Boudreaux, N. P. Liyanage, R. W. Lamb, C. E. Webster, E. T. Papish, J. H. Delcamp, *ChemCatChem* **2020**, *12*, 4879–4885.

[10] a) Y. Zhao, D. G. Truhlar, *Theor. Chem. Acc.* **2008**, *120*, 215–241; b) T. Husch, L. Freitag, M. Reiher, *J. Chem. Theory Comput.* **2018**, *14*, 2456–2468.

[11] a) C. Adamo, V. Barone, *J. Chem. Phys.* **1999**, *110*, 6158–6170; b) J. P. Perdew, K. Burke, M. Ernzerhof, *Phys. Rev. Lett.* **1996**, *77*, 3865–3868; c) J. P. Perdew, K. Burke, M. Ernzerhof, *Phys. Rev. Lett.* **1997**, *78*, 1396–1396.

[12] A. Vlcek Jr., S. Zális, *Coord. Chem. Rev.* **2007**, 251, 258–287.

[13] H. Takeda, K. Koike, H. Inoue, O. Ishitani, *J. Am. Chem. Soc.* **2008**, *130*, 2023–2031.

[14] Bruker, Madison, WI, USA, **2016**.

[15] L. Krause, R. Herbst-Irmer, G. M. Sheldrick, D. Stalke, *J. Appl. Crystallogr.* **2015**, *48*, 3–10.

[16] G. M. Sheldrick, *Acta Crystallogr. Sect. A* **2015**, *71*, 3–8.

[17] G. M. Sheldrick, *Acta Crystallogr. Sect. C* **2015**, *71*, 3–8.

[18] a) A. L. Spek, *Acta Crystallogr. Sect. E* **2020**, *76*, 1–11; b) S. Parkin, *Acta Crystallogr. Sect. A* **2000**, *56*, 317–317.

[19] A. J. C. Wilson, V. Geist, *Cryst. Res. Technol.* **1993**, *28*, 110–110.

[20] a) T. H. Dunning, *J. Chem. Phys.* **1989**, *90*, 1007–1023; b) D. Figgen, K. A. Peterson, M. Dolg, H. Stoll, *J. Chem. Phys.* **2009**, *130*, 164108; c) R. A. Kendall, T. H. Dunning, R. J. Harrison, *J. Chem. Phys.* **1992**, *96*, 6796–6806; d) A. K. Wilson, D. E. Woon, K. A. Peterson, T. H. Dunning, *J. Chem. Phys.* **1999**, *110*, 7667–7676.

[21] a) R. Bauernschmitt, R. Ahlrichs, *Chem. Phys. Lett.* **1996**, *256*, 454–464; b) M. E. Casida, C. Jamorski, K. C. Casida, D. R. Salahub, *J. Chem. Phys.* **1998**, *108*, 4439–4449; c) A. D. Laurent, D. Jacquemin, *Int. J. Quantum Chem.* **2013**, *113*, 2019–2039; d) R. E. Stratmann, G. E. Scuseria, M. J. Frisch, *J. Chem. Phys.* **1998**, *109*, 8218–8224; e) C. Van Caillie, R. D. Amos, *Chem. Phys. Lett.* **1999**, *308*, 249–255.

[22] R. A. Vogt, T. G. Gray, C. E. Crespo-Hernández, *J. Am. Chem. Soc.* **2012**, *134*, 14808–14817.

[23] J. Tomasi, B. Mennucci, R. Cammi, *Chem. Rev.* **2005**, *105*, 2999–3094.

[24] Gaussian 16, Revision C.01, M. J. Frisch, G. W. Trucks, H. B. Schlegel, G. E. Scuseria, M. A. Robb, J. R. Cheeseman, G. Scalmani, V. Barone, G. A. Petersson, H. Nakatsuji, X. Li, M. Caricato, A. V. Marenich, J. Bloino, B. G. Janesko, R. Gomperts, B. Mennucci, H. P. Hratchian, J. V. Ortiz, A. F. Izmaylov, J. L. Sonnenberg, Williams, F. Ding, F. Lipparini, F. Egidi, J. Goings, B. Peng, A. Petrone, T. Henderson, D. Ranasinghe, V. G. Zakrzewski, J. Gao, N. Rega, G. Zheng, W. Liang, M. Hada, M. Ehara, K. Toyota, R. Fukuda, J. Hasegawa, M. Ishida, T. Nakajima, Y. Honda, O. Kitao, H. Nakai, T. Vreven, K. Throssell, J. A. Montgomery Jr., J. E. Peralta, F. Ogliaro, M. J. Bearpark, J. J. Heyd, E. N. Brothers, K. N. Kudin, V. N. Staroverov, T. A. Keith, R. Kobayashi, J. Normand, K. Raghavachari, A. P. Rendell, J. C. Burant, S. S. Iyengar, J. Tomasi, M. Cossi, J. M. Millam, M. Klene, C. Adamo, R. Cammi, J. W. Ochterski, R. L. Martin, K. Morokuma, O. Farkas, J. B. Foresman, D. J. Fox, Wallingford, CT, **2016**.

Manuscript received: December 14, 2020
Revised manuscript received: January 8, 2021
Accepted manuscript online: January 11, 2021
Version of record online: ■■, ■■■

ARTICLES

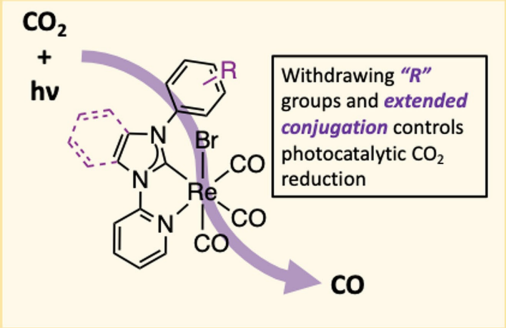

A good balance: In evaluating a series of (N-heterocyclic carbene)-rhenium catalysts for photocatalytic CO_2 reduction, the impact of electron withdrawing groups and extended conjugation showed a "sweet spot" for catalysis. This study examines the photophysical, electrochemical, and computational properties of these molecules that impact catalysis.